

Mimimal model of a quantum heat engine in a bandgap environment

Meng Xu¹, J. T. Stockburger¹, G. Kurizki² and J. Ankerhold¹

¹ Institute for Complex Quantum Systems and IQST, Ulm University -
Albert-Einstein-Allee 11, D-89069 Ulm, Germany

² Department of Chemical and Biological Physics, Weizmann Institute of Science,
Rehovot 7610001, Israel

E-mail: meng.xu@uni-ulm.de

July 2021

Abstract. An elegant realization of a quantum thermal machine is analyzed, where a two level system is embedded in an environment (reservoir) whose spectrum possesses bandgaps. The transition frequency of the system is periodically modulated so as to be in alternating spectral overlap with hot or cold reservoirs whose spectra are disjunct. Approximate and fully exact treatments supported by analytical considerations yield a complete characterization of this thermal machine operating in the deep quantum domain is provided. Strong correlations between work medium and reservoir and even between reservoirs emerge. They give rise to a rich pattern in the respective heat currents, power outputs and efficiencies from side-band resonances for slow to moderate driving frequencies with reservoirs still close to equilibrium to collective nonlinear resonances appearing for fast driving with reservoirs pushed to non-equilibrium.

Keywords: Quantum thermal machines, quantum heat transport, non-perturbative open quantum dynamics

1. Introduction

The description of macroscopic, classical thermal machines is based on the assumption that their dynamics is adiabatic, i.e. represented by a sequences of equilibrium states [1, 2]. In recent years, it has turned out that the application of these concepts in the quantum domain does not necessarily lead to heat machines whose operation is substantially governed by the laws of quantum mechanics [3]. First steps towards truly non-equilibrium descriptions of thermal machines in the quantum domain have been made mostly within the framework of Born-Markov master equations and very often under idealized conditions, where, for example, individual strokes are treated independently and are then are “glued” together to a full cycle. This in turn requires basically complete thermalization and separability in the appropriate strokes, thus remaining within the paradigm of classical thermodynamics.

In general, the dynamics of quantum thermal machines must be placed within the context of open quantum systems, where non-separability is generic at low temperatures and correlations between the working medium (WM henceforth) and the reservoirs inevitably affect the operation. In this respect, fascinating progress has been achieved very recently in several directions revealing, for example, that non-Markovianity can be beneficial [4] and that switching on and off the WM coupling to the reservoirs has to be an integral part of the full dynamics with strong influences on power output and efficiency [5, 6], or that coherences may be maintained as a resource [7]. Along with these developments, non-perturbative treatments of the non-equilibrium quantum dynamics have been established, such as generalized master-Floquet equations [8] and exact approaches based on the path integral representation of the reduced density operator of the WM [9]. Among the latter treatments one finds specifically the Hierarchy of Equations of Motion (HEOMs) [10, 11], the Stochastic Liouville-von Neumann Equation (SLN) [12, 13], the multilayer multiconfiguration time-dependent Hartree (ML-MCTDH) approach [14–16], and the continuous-time quantum Monte Carlo (CT-QMC) algorithm [17, 18] that have been recently applied to explore quantum heat phenomena. This in turn paves the way to explore the rich world of quantum thermodynamics far from equilibrium, at low temperatures, and the presence of mesoscopic or microscopic reservoirs.

Experimentally, classical single-atom heat engines have been realised with trapped single calcium ions as WM [19]. Studies of quantum heat engines include also other platforms such as superconducting circuits with electronically engineered reservoirs [20–25], nitrogen vacancy centers in diamond coupled to nuclear spin baths [3], phonon reservoirs in solid state circuits [26], carbon nanotubes acting as mechanical resonators [27] as well as spin-wave or phonon-reservoirs in systems of trapped ions [28]. Although remarkable in terms of control and fabrication, the performance of these machines is mostly limited to the domain of classical thermodynamics or only exhibit limited quantum effects. Theoretical proposals have been put forward to boost quantum advantages or better understand design principles which support strongly quantum properties [1, 2, 4, 5, 29–33]. In particular, such quantum properties may be of interest in the context of theoretical demonstrations that non-overlapping spectra of thermal reservoirs allow for minimal settings of quantum heat machines [4, 34–38], where on-off-switching of the thermal couplings is not required. This is not only a great conceptual advantage compared to conventional protocols, for example, a four stroke quantum Otto engine [5, 6], but also more convenient for experimental realizations.

In the following, we consider, as illustrated in Fig. 1, a two level system (qubit) whose transition frequency is periodically modulated such that it is in alternating spectral overlap with either the hot or the cold reservoir whose spectra possess bandgaps. Bandgap reservoirs arise in photonic crystals [39, 40] but can also be realized in superconducting circuits by placing transmission lines or LC-oscillators as interfaces between transmon qubits and ohmic resistors. To augment quantum effects, we consider strong system-reservoir coupling and take the cold reservoir to be at zero temperature

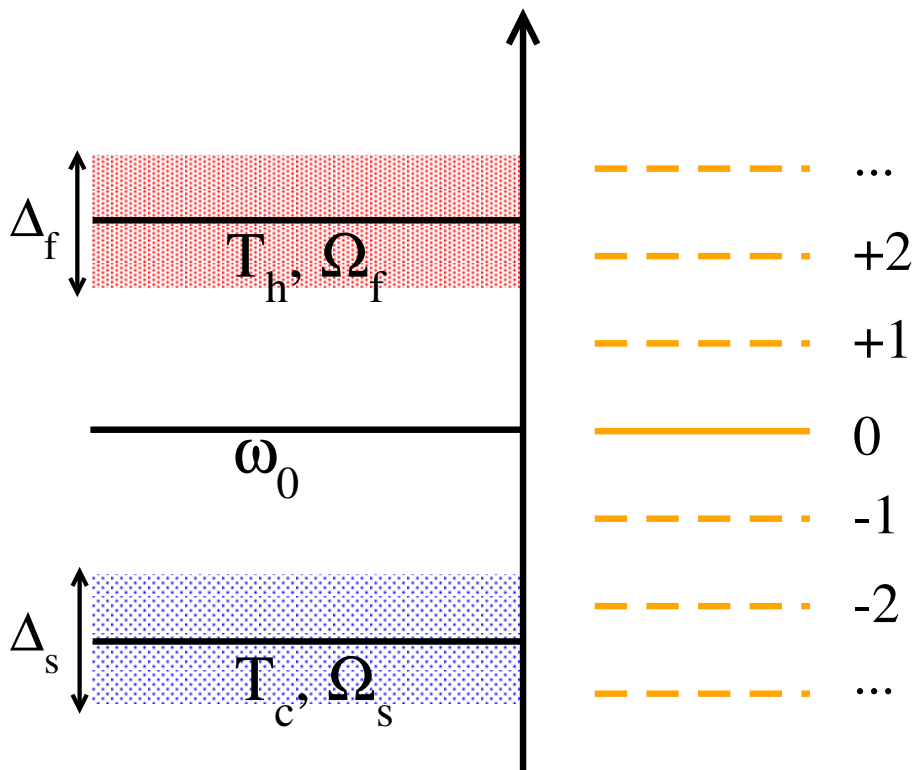


Figure 1. A schematic view of the proposed quantum thermal machine in the frequency domain. The transition frequency of a two level system (TLS) with static level spacing ω_0 is periodically modulated as $\omega(t) = \omega_0 + \lambda \cos(\omega_s t)$ [see Eq. (2)]. This modulation gives rise to side-bands $k\omega_s, k \in \mathcal{Z}$ (orange). In this way, the TLS realizes a working medium that interacts continuously with two reservoirs at different temperatures $T_h > T_c$ having localized spectral distributions at low frequencies around Ω_s (slow bath) and at high frequencies around Ω_f (fast bath) with respective bandwidths Δ_α .

($T_c = 0$). In this way, we reveal highly nontrivial features such as anharmonicity, non-equilibration due to finite time cycles as well as quantum coherences and correlations within an architecture which allows for detailed understanding. For this purpose we evoke the HEOM approach [10, 41–44], a non-perturbative simulation technique of open quantum systems which is derived from the formally exact representation of the reduced density matrix in terms of path integrals [9, 45]. The HEOM has the additional benefit that, as part of the hierarchy, perturbative approaches such as the Redfield and the Lindblad master equations can be easily computed by the same code. In particular, the first order truncation of HEOM gives a generalized time-nonlocal master equation which allows us to find asymptotic Floquet states within a non-Markovian, perturbative method [46, 47]. By comparing the results of these various approaches, insight is provided into the applicability of the perturbative treatments and the relevance of higher order quantum correlations.

This paper is arranged as follows. In Sec. 2, we present the heat engine model, whose operation essentially depends on the designed reservoir spectra. In Sec. 3, we

outline the exact HEOM approach, its approximated treatment, and its use to extract heat currents. The central part is given in Sec. 4, where we present the simulation results. We first compare the results of the Redfield-plus approximation with HEOM, then study the quantum heat engine performance as a function of the modulation rate and other parameters such as the thermal coupling strengths. The conclusions are presented in Sec. 5.

2. Two state thermal machine

Quantum heat engines (QHEs) can be theoretically studied within the framework of open quantum dynamics[5, 29, 30, 34, 47–51]. Within this framework, the total Hamiltonian consists of three parts,

$$H(t) = H_0(t) + H_I + H_B , \quad (1)$$

where $H_0(t)$ pertains to a system that acts as WM subject to external driving [22, 52], H_B represents two thermal reservoirs (baths) at temperatures, $T_h > T_c$, henceforth denoted as hot reservoir and cold reservoir temperatures, respectively, and H_I is the coupling between the WM and the reservoirs. Here, we consider a paradigmatic WM, namely, a TLS with periodic frequency modulation, i.e.,

$$H_0(t) = \hbar\omega(t)\sigma_+\sigma_- , \quad (2)$$

with $\sigma_{\pm} = \frac{1}{2}(\sigma_x \pm i\sigma_y)$ written in terms of the Pauli matrices σ_n , $n = x, y, z$. The modulation of the transition frequency is taken to be of the form

$$\omega(t) = \omega_0 + \lambda \cos(\omega_s t) , \quad (3)$$

whose amplitude λ and driving frequency ω_s are the main variable parameters in the following analysis. We shall $\hbar = k_B = 1$. In the context of a thermal machine, the situation, where $\omega(t) < \omega_0$ corresponds to an expansion of the WM, while $\omega(t) > \omega_0$ represents its compression. Within the set-up illustrated in Fig. 2, a conventional heat engine then operates such that the low (high) frequency bath has the lower (higher) temperature T_c (T_h). However, we will also consider the reversed situation and demonstrate that it may induce even stronger heat fluxes.

The bare system Hamiltonian is diagonal in the eigenbasis of $\sigma_+\sigma_- = (\sigma_z + 1)/2$, i.e. $\sigma_+\sigma_-|q\rangle = q|q\rangle$ with $q = 0, 1$. Consequently, the bare system time evolution operator $\mathcal{U}(t) = \mathcal{T} \exp[-i \int_0^t d\tau H_0(\tau)]$ can easily be expressed as

$$\begin{aligned} \mathcal{U}(t) &= \exp \left\{ -i \int_0^t d\tau [\omega_0 + \lambda \cos(\omega_s \tau)] \sigma_+\sigma_- \right\} \\ &= \sigma_- \sigma_+ + \sigma_+ \sigma_- \sum_{k=-\infty}^{+\infty} J_k \left(\frac{\lambda}{\omega_s} \right) e^{-i\omega^{(k)} t} , \end{aligned} \quad (4)$$

where $\omega^{(k)} = \omega_0 + k\omega_s$ are the quasi-energies (denoted by orange lines in Fig. 1) and $J_k(\cdot)$ are Bessel functions of the first kind. The WM has thus multiple equidistant quasi-energy levels (in agreement with Floquet theory) which, as we will show, has prominent effects on quantum heat transport. For $\lambda/\omega_s \rightarrow 0$ one has $J_{|k| \neq 0}(\lambda/\omega_s) \rightarrow 0$, $J_0(\lambda/\omega_s) \rightarrow 1$ so that the system effectively reduces to a static system with level spacing ω_0 .

As thermal reservoirs we consider quasi-continua of independent harmonic degrees of freedom with localized spectral distributions, namely, a slow bath H_s composed of oscillators in the frequency range below ω_0 and a fast bath H_f with oscillator frequencies above ω_0 . Accordingly, one can write

$$\begin{aligned} H_B &= H_s + H_f \\ &= \sum_{\alpha=s,f} \left\{ \sum_{i=1}^{\infty} \frac{p_{\alpha,i}^2}{2m_{\alpha,i}} + \frac{1}{2} m_{\alpha,i} \omega_{\alpha,i}^2 x_{\alpha,i}^2 \right\}, \end{aligned} \quad (5)$$

where $m_{\alpha,i}$, $\omega_{\alpha,i}$, $x_{\alpha,i}$ and $p_{\alpha,i}$ denote the mass, frequency, coordinate and momentum of the i th oscillator in the α th reservoir. The bilinear interaction between these reservoirs and the WM is given by

$$H_I = \sum_{\alpha=s,f} X_{\alpha} \sigma_x + \frac{1}{2} \sum_{\alpha=s,f} \mu_{\alpha}, \quad (6)$$

with $X_{\alpha} = \sum_i c_{\alpha,i} x_{\alpha,i}$ denoting a collective coordinate of the α th reservoir and $c_{\alpha,i}$ being the coupling constant of the i th mode with α . The last term guarantees that the reservoirs only act dynamically upon the system without any coupling-induced distortion of the system. We note that the total Hamiltonian in Eq. (1) can be transformed into the form of the conventional spin-boson model [9] by the canonical transformation $\tilde{H}(t) = SH(t)S^{\dagger}$ with $S = \frac{1}{2}(\sigma_x + \sigma_z)$ which implies $\sigma_z \rightarrow \tau_x$ and $\sigma_x \rightarrow \tau_z$, where τ_k denote Pauli matrices in the rotated basis.

The effect of the two reservoirs on the WM is completely described by the coupling weighted spectral densities summed over all modes

$$J_{\alpha}(\omega) = \frac{\pi}{2} \sum_i \frac{c_{\alpha,i}^2}{m_{\alpha} \omega_{\alpha,i}} \delta(\omega - \omega_{\alpha,i}) \quad (7)$$

which leads to $\mu_{\alpha} = (2/\pi) \int_0^{\infty} d\omega J_{\alpha}(\omega)/\omega$. According to our setting of two reservoirs with localized spectral distributions and only negligible overlap among them, the following continuum form of spectra is convenient, i.e.,

$$J_{\alpha}(\omega) = \frac{\kappa_{\alpha} \xi_{\alpha}^8 \omega}{(\omega^2 - \Omega_{\alpha}^2)^6 + \omega^2 \xi_{\alpha}^{10}}, \quad \alpha = s, f \quad (8)$$

with central frequencies $\Omega_f > \omega_0 > \Omega_s$ and frequency scales ξ_{α} which determine the widths Δ_{α} of the spectral distributions. In what follows, all masses are set to unity and all frequencies are scaled with $\xi_s = \xi_f$ so that the dimensionless bandwidths Δ_{α} are of

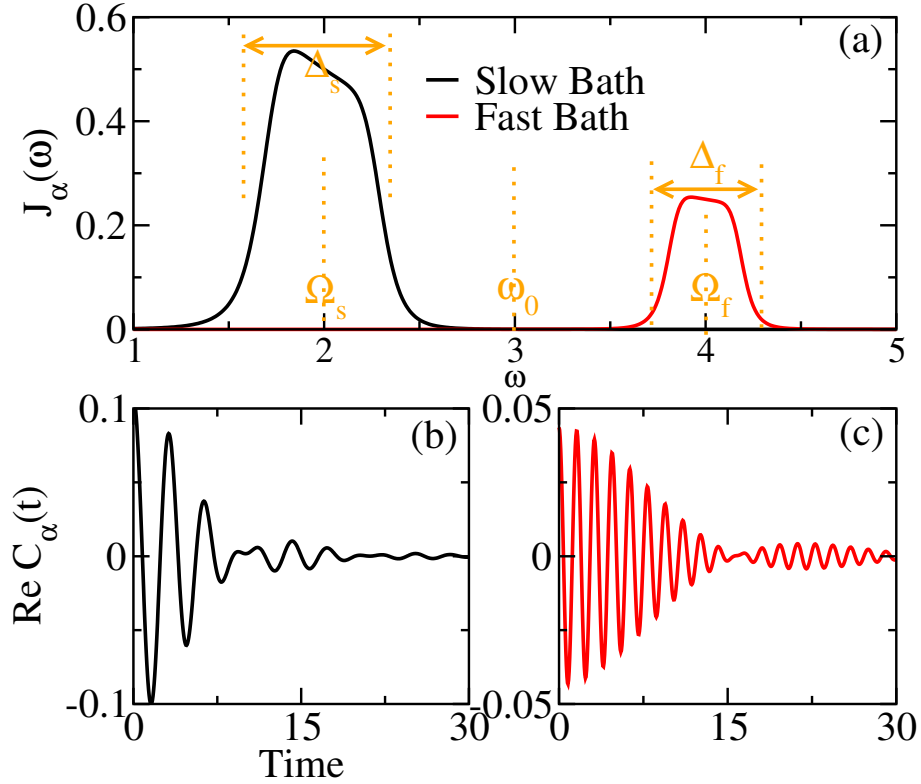


Figure 2. Non-overlapping spectral densities separated by a bandgap as in Fig. 1 for two thermal reservoirs interacting with a frequency modulated TLS with static transition frequency ω_0 (a). The real parts of the corresponding correlation functions are shown $C_\alpha(t)$ for the slow (b) and the fast (c) bath. The parameters are: $\kappa_s = \kappa_f = 1.0$, $(\Omega_s, T_c) = (2.0, 0.0)$, and $(\Omega_f, T_h) = (4.0, 2.0)$.

order unity. The WM continuously interacts with the reservoirs with varying spectral overlap due to the external driving (see Figs. 1 and 2). At resonance, the effective couplings read

$$\kappa_\alpha^{\text{eff}} = \frac{J_\alpha(\Omega_\alpha)}{\Omega_\alpha} = \frac{\kappa_\alpha}{\Omega_\alpha^2}. \quad (9)$$

As noted above, in order to focus on the quantum regime with strong non-Markovian effects, we consider the cold reservoir to have $T_c = 0$. This immediately implies that our machine cannot be a quantum refrigerator.

3. Simulation Techniques

The described setting is highly non-trivial, first, because we consider localized, non-overlapping reservoir (bath) spectra and the machine is operated at low temperatures. Hence, correlations between WM and the thermal reservoirs are expected to be so strong that conventional master equations are not applicable. We thus rely on the exact quantum dynamical simulations within the Hierarchical Equation of Motion (HEOM) approach.

3.1. Hierarchical equation of motion

Here, we briefly describe the essence of the HEOM approach and its derivation from the path integral expression of the reduced density matrix. For the sake of simplicity, we consider only a single reservoir for a Hamiltonian of the form (5) and assume factorized initial states at the time zero $t = 0$, $\rho_T(0) = \rho_m(0) \otimes e^{-\beta H_B}/Z_B$, where $Z_B = \text{Tr} e^{-\beta H_B}$ and ρ_m is the density operator of the relevant system (WM). The generalization to correlated initial states has also been discussed [53, 54].

In path integral representation [45] the reduced density operator is obtained as

$$\rho_m(t) = \int \mathcal{D}q^+(t) \mathcal{D}q^-(t) e^{i\{S_+[q^+(t)] - S_-[q^-(t)]\}} \mathcal{F}[\sigma_x^+(t), \sigma_x^-(t)] \rho_m(0) . \quad (10)$$

Generally, a continuous system coordinate can be discretized using a system-specific discrete variable representation (DVR) [55]. Within the HEOM and for the TLS-WM considered here, a representation in terms of the eigenstates $|q\rangle \in \{|0\rangle, |1\rangle\}$ is convenient. The coordinates $q^+(t)$ and $q^-(t)$ denote forward and backward system paths, respectively, and $S_{\pm}[q^{\pm}(t)]$ the corresponding actions,

$$S_{\pm}[q^{\pm}(t)] = - \int_0^t d\tau \omega(\tau) q^{\pm}(\tau) . \quad (11)$$

These paths $q^{\pm}(t)$ directly determine also the $\sigma_x^{\pm}(t)$ according to

$$\sigma_x^{\pm}(t) = \langle q^{\pm}(t^+) | \sigma_x | q^{\pm}(t) \rangle , \quad (12)$$

where t^+ denotes the time slice on the forward and backward paths that follows the time slice t .

The effective impact of the reservoir onto the system dynamics is described by the influence functional [45] which reads

$$\begin{aligned} \mathcal{F}[\sigma_x^+(t), \sigma_x^-(t)] = \exp \left\{ - \int_0^t ds [\sigma_x^+(s) - \sigma_x^-(s)] \right. \\ \left. \times \int_0^s d\tau [C(s - \tau) \sigma_x^+(\tau) - C^*(s - \tau) \sigma_x^-(\tau)] \right\} . \end{aligned} \quad (13)$$

The derivation of the real-time HEOM starts by first expanding [10, 56] or fitting [57, 58] the bath correlation function as a sum of exponential terms, i.e.

$$\begin{aligned} C(t) &= \frac{1}{Z_B} \text{Tr}_B [e^{-\beta H_B} X(t) X(0)] \\ &= \int_{-\infty}^{+\infty} \frac{d\omega}{\pi} J(\omega) n_{\beta}(\omega) e^{-i\omega t} \\ &= \sum_k d_k e^{-\gamma_k t} \quad \text{for } t > 0 \end{aligned} \quad (14)$$

with the collective bath operator X as in Eq. (6) and the Bose-Einstein distribution $n_{\beta}(\omega) = 1/(1 - e^{-\beta\omega})$. Accordingly, the spectral function $S(\omega) = J(\omega) n_{\beta}(\omega)$ obeys

$S(\omega) = S(-\omega) + J(\omega)$ with $J(-\omega) = -J(\omega)$ as in Eq. (8). The d_k in (14) denote proper coefficients in an expansion in terms of exponentials with proper coefficients γ_k . All characteristics of the reservoirs are expressed by the correlation functions which are depicted in Fig. 2 for the slow and fast reservoirs in Eq. (8), respectively. In contrast to conventional Ohmic-type spectral distributions $J(\omega) \propto \omega$ that at higher temperatures lead to an exponential decay of the auto-correlation $C(t)$, we here observe long correlation times $\tau_R \gtrsim 30$ (in arbitrary units) that exceed the driving (modulation) periods $\tau_S = 2\pi/\omega_s$ if $\omega_s \gtrsim 2\pi/\tau_R \approx 0.2$. Consequently, a separation of time scales on which Markovian perturbative approaches are based, does not exist and memory effects are strong as we will see below. The limited bandwidth of the reservoirs yields beating patterns, particularly for the high frequency bath.

By resorting to the following auxiliary density operator (ADO) definition,

$$\rho_{\mathbf{n}}(t) = \int \mathcal{D}q^+(t)\mathcal{D}q^-(t)e^{i\{S_+[q^+(t)]-S_-[q^-(t)]\}} \prod_k [\phi_k(t)]^{n_k} \mathcal{F}[\sigma_x^+(t), \sigma_x^-(t)] \rho_m(0) ; \quad (15a)$$

$$\phi_k(t) = -i \int_0^t ds \left[\sigma_x^+(s) d_k e^{-\gamma_k(t-s)} - \sigma_x^-(s) d_k^* e^{-\gamma_k(t-s)} \right] , \quad (15b)$$

the HEOM formulation leads to the equation of motion [10, 41, 42, 59–63]

$$\begin{aligned} \frac{d\rho_{\mathbf{n}}(t)}{dt} = & - \left(i\mathcal{L}_0(t) + \sum_k n_k \gamma_k \right) \rho_{\mathbf{n}}(t) - i \left[\sigma_x, \sum_k \rho_{\mathbf{n}_k^+}(t) \right] \\ & - i \sum_k n_k \left(d_k \sigma_x \rho_{\mathbf{n}_k^-}(t) - d_k^* \rho_{\mathbf{n}_k^-}(t) \sigma_x \right) , \end{aligned} \quad (16)$$

which shows that the WM interacts via σ_x with the collective bath force. The ADOs $\rho_{\mathbf{n}}$ s are labeled by the subscript \mathbf{n} denoting a set of integers $\{n_1, \dots, n_k, \dots\}$, with $n_k \geq 0$ associated with the k th exponential term in Eq. (14); \mathbf{n}_k^+ and \mathbf{n}_k^- denote $\{n_1, \dots, n_k + 1, \dots\}$, and $\{n_1, \dots, n_k - 1, \dots\}$, respectively. The super-operator acting on these ADO is defined as $\mathcal{L}_0(t)\rho_{\mathbf{n}} = [H_0(t), \rho_{\mathbf{n}}]$. The WM reduced density operator in this notation is $\rho_m = \rho_{\{0, \dots, 0, \dots\}}$.

Assuming that $\rho_0(t)$ is of order one, the magnitude of $\rho_{\mathbf{n}}(t)$ is proportional to $\prod_k d_k^{n_k}$, which may be divergent for strong system-bath coupling η as $|\mathbf{n}| \doteq n_1 + n_2 + \dots + n_k + \dots$ increases. Therefore, the original HEOM [10, 64] is re-scaled and combined with on-the-fly filtering methods [65] to solve this problem efficiently. In our simulations, we choose the following rescaling,

$$\tilde{\rho}_{\mathbf{n}}(t) = \left(\prod_k n_k! |d_k|^{n_k} \right)^{-1/2} \rho_{\mathbf{n}}(t) , \quad (17)$$

so that Eq. (16) is recast as

$$\begin{aligned} \frac{d\tilde{\rho}_{\mathbf{n}}(t)}{dt} = & - \left(i\mathcal{L}_0(t) + \sum_k n_k \gamma_k \right) \tilde{\rho}_{\mathbf{n}}(t) - i \sum_k \sqrt{(n_k + 1)|d_k|} \left[\sigma_x, \tilde{\rho}_{\mathbf{n}_k^+}(t) \right] \\ & - i \sum_k \sqrt{\frac{n_k}{|d_k|}} \left(d_k \sigma_x \tilde{\rho}_{\mathbf{n}_k^-}(t) - d_k^* \tilde{\rho}_{\mathbf{n}_k^-}(t) \sigma_x \right) , \end{aligned} \quad (18)$$

The magnitude of $\tilde{\rho}_{\mathbf{n}}(t)$ is proportional to $\prod_k \sqrt{|d_k|^{n_k}/n_k!}$ and decays to zero for high hierarchical levels. Therefore, we can set $\rho_{\mathbf{n}}(t) = 0$ if $|\rho_{\mathbf{n}}^{\max}(t)| < \delta$, where δ denotes the error tolerance (here we set $\delta = 10^{-7}$). More advanced algorithms to support the efficiency and numerical stability can be found in Refs. [42, 61–63, 66–69].

According to (18) we expect the reduced density to approach a periodic steady state $\rho_m(t) \rightarrow \rho_m^{(st)}(t) = \rho_m^{(st)}(t + \tau_s)$ with $\tau_s = 2\pi/\omega_s$ being the driving (modulation) period. This periodicity characterizes all single time-dependent observables (one-point correlations) such as the excited state population $P_1(t) = \langle \sigma_+ \sigma_- \rangle_t$ or the heat currents $I_\alpha(t)$.

3.2. Perturbative treatment

Approximate treatments of open system dynamics have been developed to second order in the system-reservoir coupling. Together with a time scale separation between fast decaying reservoir correlations and relaxation dynamics of the reduced density operator, this leads to the Redfield master equation [70]. Interestingly, an extended Redfield equation is also obtained from the HEOM if it is curtailed at first-order, i.e. restricted to ADOs with $\sum_k n_k = 1$. Namely, in the interaction picture this Redfield equation has the form

$$\frac{d}{dt}\rho_m^I(t) = -i \sum_k [\sigma_x^I(t), \rho_{\mathbf{0}_k^+}^I(t)] , \quad (19a)$$

$$\frac{d}{dt}\rho_{\mathbf{0}_k^+}^I(t) = -\gamma_k \rho_{\mathbf{0}_k^+}^I(t) - i[d_k \sigma_x^I(t) \rho_m^I(t) - d_k^* \rho_m^I(t) \sigma_x^I(t)] , \quad (19b)$$

where $\sigma_x^I(t)$, $\rho_s^I(t)$ and $\rho_{\mathbf{0}_k^+}^I(t)$ denote the system (WM), reduced density matrix and first-order ADOs in the interaction picture, respectively. Note that Eqs. (19a) and (19b) have the same structure as their counterparts in the generalized Floquet theory [46, 47, 50]. Upon solving Eq. (19b) and inserting it into Eq. (19a), one has

$$\begin{aligned} \frac{d}{dt}\rho_m^I(t) &= - \sum_k \int_0^t d\tau e^{-\gamma_k(t-\tau)} [\sigma_x^I(t), d_k \sigma_x^I(\tau) \rho_m^I(\tau) - d_k^* \rho_m^I(\tau) \sigma_x^I(\tau)] \\ &= - \int_0^t d\tau [\sigma_x^I(t), C(t-\tau) \sigma_x^I(\tau) \rho_m^I(\tau) - C^*(t-\tau) \rho_m^I(\tau) \sigma_x^I(\tau)] \\ &= - \int_0^t d\tau \text{Tr}_B \{ [H_I^I(t), [H_I^I(\tau), \rho_T^I(\tau)]] \} . \end{aligned} \quad (20)$$

In the above expression, the correlation function in Eq. (14) and the Born approximation [70] have been used but *not* the Markov approximation. Thus, Eq. (20) is an integro-differential equation nonlocal in time which is henceforth denoted *Redfield-plus* (Redfield⁺) to distinguish it from the conventional Redfield formulation. It can be conveniently solved with the help of auxiliary variables [58, 71, 72].

In the Markov limit one sets in Eq. (20) $\rho_m^I(\tau) \rightarrow \rho_m^I(t)$, leading to the conventional time-local Redfield master equation

$$\frac{d}{dt}\rho_m^I(t) = - \int_0^t d\tau \text{Tr}_B \{ [H_I^I(t), [H_I^I(\tau), \rho_T^I(t)]] \} . \quad (21)$$

This equation can be easily solved in the time domain with the help of Eq. (14) through the use of the auxiliary operator

$$q_k^I(t) = -i \int_0^t d\tau d_k e^{-\gamma_k(t-\tau)} \sigma_x^I(\tau) . \quad (22)$$

This substitution transforms Eq. (21) into

$$\frac{d}{dt} \rho_m^I(t) = -i \sum_k [\sigma_x^I(t), q_k^I(t) \rho_m^I(t) + \rho_m^I(t) q_k^{I*}(t)] ; \quad (23a)$$

$$\frac{d}{dt} q_k^I(t) = -\gamma_k q_k^I(t) - i d_k \sigma_x^I(t) . \quad (23b)$$

Due to the strong non-Markovian effects (see Fig. 2) of the bath considered in the present paper, the Redfield master equation becomes invalid. Therefore, the HEOM approach can be seen as an infinite-order extension of the Redfield-plus/Redfield approximation [60, 73, 74]. This allows us to reveal consistently the impact of higher order system-reservoir correlations which are particularly subtle for heat currents.

3.3. Heat current

In the framework of the HEOM, effects of the environment on the system dynamics can be obtained from the ADOs [43, 44, 75–77]. Here, we concentrate on the quantum heat current which is linear in the collective bath force X . One starts, in the interaction picture, with the following two equations

$$\frac{d}{dt} \rho_m^I(t) = -i \sum_k [\sigma_x^I(t), \rho_{\mathbf{0}_k^+}^I(t)] ; \quad (24a)$$

$$\frac{d}{dt} \rho_m^I(t) = -i \text{Tr}_B \{ [\sigma_x^I(t) X^I(t), \rho_T^I(t)] \} = -i [\sigma_x^I(t), \text{Tr}_B \{ X^I(t) \rho_T^I(t) \}] , \quad (24b)$$

where $\rho_T^I(t)$ denotes the total density matrix in the interaction picture. In the next step, relations between first-order ADOs ($\rho_{\mathbf{0}_k^+}$) in the HEOM and first-order moments of X are constructed according to

$$\sum_k \rho_{\mathbf{0}_k^+}^I(t) = \text{Tr}_B \{ X^I(t) \rho_T^I(t) \} . \quad (25)$$

Higher-order relations can be found in Refs. [44, 75].

In the presence of two thermal reservoirs, the above relation is inserted into the definition [15, 44, 78] in the quantum heat current $I_\alpha(t)$ between the quantum system and the α th bath, i.e.

$$\begin{aligned} I_\alpha(t) &\equiv -\frac{d}{dt} \langle H_\alpha + H_{I,\alpha} \rangle = -i \langle [H_0(t), \sigma_x X_\alpha] \rangle \\ &= -i \text{Tr}_m \{ [H_0(t), \sigma_x] \text{Tr}_B \{ X_\alpha \rho_T \} \} \\ &= -\omega(t) \sum_k \text{Tr}_m \{ \sigma_y \rho_{\mathbf{0}_k^+}(t) \} , \quad k \in \alpha \text{th bath} . \end{aligned} \quad (26)$$

Here, $H_{1,\alpha}$ denotes the coupling between the system and the α -th reservoir. By definition, a positive value of $I_\alpha(t)$ corresponds to energy flowing into system, while a negative value corresponds to its inverse.

Deeper insight into the operation of the thermal machine in the quantum regime is given by the normalized correlations between the slow and the fast reservoir modes mediated by the driven two level WM which can be easily obtained from the HEOM, i.e.

$$\langle X_s^I X_f^I \rangle_t = \frac{1}{C_s(0)C_f(0)} \sum_{k,l} \text{Tr}_m \{ \rho_{\mathbf{0}_k^+, \mathbf{0}_l^+}^I(t) \} , \quad (27)$$

with k, l denoting slow and fast baths effective modes, respectively. These correlations are not present in the classical treatment nor in the standard Redfield master equation.

In steady state, we have $\rho_{\mathbf{n}}^{sst}(t) = \rho_{\mathbf{n}}^{sst}(t + \tau_s)$, and also $I_\alpha^{sst}(t) = I_\alpha^{sst}(t + \tau_s)$. It is thus convenient to define

$$\bar{I}_\alpha = \lim_{t \rightarrow \infty} \frac{1}{\tau_s} \int_t^{t+\tau_s} d\tau I_\alpha^{sst}(\tau) \quad (28)$$

as an average of the heat current over one driving period. When representing the current as $I_\alpha^{st}(t) = \sum_m \mathcal{I}_{\alpha,m} \exp(-im\omega_s t)$, this then implies $\bar{I}_\alpha = \mathcal{I}_{\alpha,0}$.

With the above set of equations at hand, we are in a position to explore heat transfer properties of the quantum heat engine in more detail.

4. Simulation results

In this section, we present numerical results based on the HEOM and the approximate treatments Redfield⁺ and Born-Markov Redfield, respectively. The total initial density matrix is taken to be a factorized, state i.e. $\rho_T(0) = \rho_m(0) \otimes \prod_\alpha e^{-\beta_\alpha H_\alpha} / \text{Tr}[e^{-\beta_\alpha H_\alpha}]$, whose time evolution is followed until a steady state is approached. In this regime, observables are calculated for various parameter sets, where thermal reservoirs are characterized by their temperature and central frequency (Ω_α, T_i) , $\alpha = s, f$ and $i = h, c$ while bandwidths Δ_α are kept constant throughout. In particular, we consider two situations: (i) the hot reservoir is represented by the slow-mode reservoir and the cold one by the fast reservoir, i.e. (Ω_s, T_h) and (Ω_f, T_c) and (ii) the reversed case (Ω_s, T_c) and (Ω_f, T_h) .

As a first step, we compare data obtained from the approximate treatment with exact ones from the HEOM. The task is to find parameter domains for which the Redfield⁺ is sufficiently accurate and conversely to identify, where it fails due to very strong WM-reservoirs correlations (strong non-Markovianity). Further insights into the resonance pattern of the heat current are then obtained. For those parameters, where Redfield⁺ can be applied, properties of the continuous-cycle QHE are explored as a function of the temperature gradient, the modulation amplitude, and the system bath coupling strength.

In the numerical simulations, the spectral function $S(\omega) = J(\omega)n_\beta(\omega)$ is properly fitted to an optimized rational function with tolerance $\delta_S \leq 10^{-6}$ and then Fourier

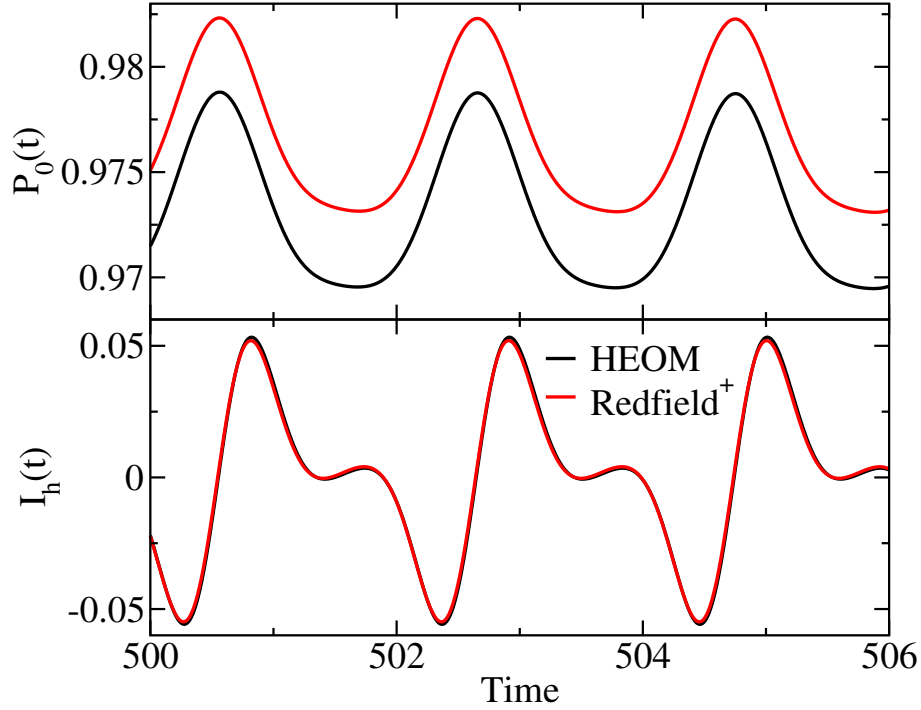


Figure 3. Time-dependent dynamics of the ground-state population of the WM (top) and of the heat current $I_h(t)$ (bottom) in periodic asymptotic (steady) state simulated by HEOM and Redfield⁺. The simulation parameters are (in a.u.): $\omega_0 = 3.0$, $\lambda = 1.0$, $\kappa_\alpha = 1.0$, $\omega_s = 3.0$, $(\Omega_s, T_c) = (2.0, 0.0)$, and $(\Omega_f, T_h) = (4.0, 2.0)$.

transformed to correlation functions $C(t)$ written as a sum of exponential terms. Concurrently, and on-the-fly filtering [65] algorithm is adopted in order to achieve high efficiency. Atomic units (a.u.) are used here in order to treat a variety of regimes.

4.1. Perturbative versus exact treatment

In Figs. 3 to 7 we compare the performance of the perturbative Redfield⁺ with the exact HEOM for various observables. The general outcome of this comparative analysis is that we can identify parameter regimes, where the approximate treatment provides quantitatively excellent results at least for heat currents. While Redfield⁺ accounts to some extent for memory effects in the thermal reservoirs, it does so for sufficiently weak system-bath interaction. Consequently, the dynamics of the system operator in Eq. (20) $\sigma_x(t)$ reflects the bare dynamics, i.e.,

$$\begin{aligned} \sigma_x(t) &= \mathcal{U}^\dagger(t) \sigma_x \mathcal{U}(t) \\ &= \sum_k J_k \left(\frac{\lambda}{\omega_s} \right) \left[\sigma_+ e^{i\omega^{(k)}t} + \sigma_- e^{-i\omega^{(k)}t} \right]. \end{aligned} \quad (29)$$

However, for stronger WM-reservoir coupling (thermal contact) and/or long correlation time of the reservoir, this bare dynamics is influenced by higher order correlations between WM and reservoirs (see below). This includes higher order quanta exchange

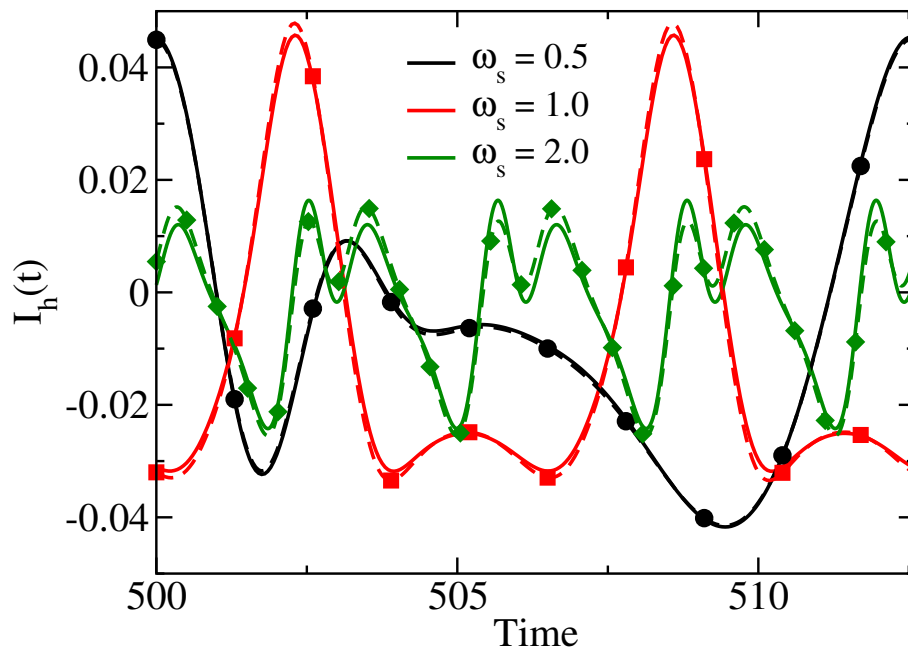


Figure 4. Heat current dynamics $I_h(t)$ in periodic steady state simulated by HEOM (dashed lines) and Redfield⁺ (solid lines) for various driving frequencies. The simulation parameters are (in a.u.): $\omega_0 = 3.0$, $\lambda = 1.0$, $\kappa_\alpha = 1.0$, $(\Omega_s, T_c) = (2.0, 0.0)$, and $(\Omega_f, T_h) = (4.0, 2.0)$.

between the periodically driven TLS and the reservoir oscillator modes with frequencies around Ω_s and Ω_f , respectively.

We start in Fig. 3 with the dynamics of the ground state population and the heat current $I_h(t)$ in the periodic steady state with period τ_s . Although Redfield⁺ predicts a somewhat higher population than HEOM, the heat currents obtained by the two methods are in excellent agreement for the chosen parameters of relatively strong and fast driving (see Fig. 4).

This is true of the mean quantities \bar{I}_c, \bar{I}_h depicted in Fig. 5(b). A resonance-like pattern is apparent when ω_s is tuned away from the regime of very slow (adiabatic) driving to the fast driving regime which is quantitatively reproduced by Redfield⁺. However, as expected, the agreement is less good when we interchange the reservoir temperatures such that the high frequency bath becomes the cold (hot) reservoir and the low-frequency reservoir the hot one, see Fig. 6. Hence, non-Markovian effects are strongly enhanced at high frequencies which renders the Redfield⁺ inadequate. It reproduces the resonance pattern qualitatively, but their respective widths and magnitudes are quantitatively wrong. We will discuss below the deeper reason for this mismatch, but can already emphasize here, that the full quantum descriptions predicts *larger* absolute heat fluxes.

Even when the parameter set of Fig. 5 is adopted for the reservoirs, but the driving amplitude for the WM is substantially increased, see Fig. 7, the performance of Redfield⁺ remains acceptable with minor deviations from HEOM only in the resonance range at

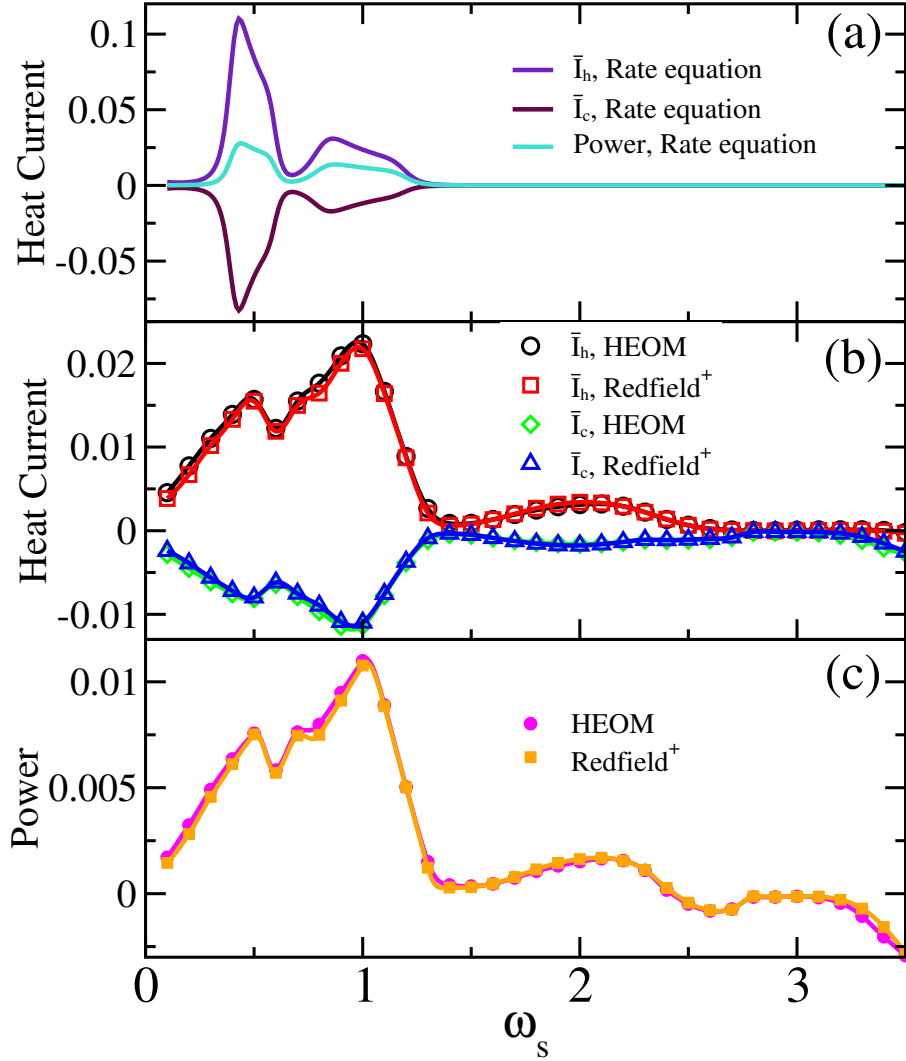


Figure 5. Mean heat current versus driving frequency in the Born-Markov approximation (a) and according to the method of Redfield⁺ and HEOM (b). The net power corresponding to (b) is depicted (c). The simulation parameters are the same as in Fig. 4.

slower driving frequencies again with the overall tendency to yield smaller absolute values for heat currents.

Based on the above studies (and more systematic results that are not shown here), we conclude that for the setting studied here the Redfield⁺ is quantitatively correct in the range of driving frequencies $0 \leq \omega_s \lesssim \omega_0$ and for driving amplitudes $\lambda \lesssim |\Omega_f + \Delta_f/2 - \omega_0|, |\Omega_s - \Delta_f/2 - \omega_0|$ (so that $\omega(t)$ does not exceed the full bandwidths of the reservoirs during one period) as long as Ω_f/T is on the order of 1 with T being the temperature of the high frequency reservoir (i.e. the reservoir memory time is not too strong).

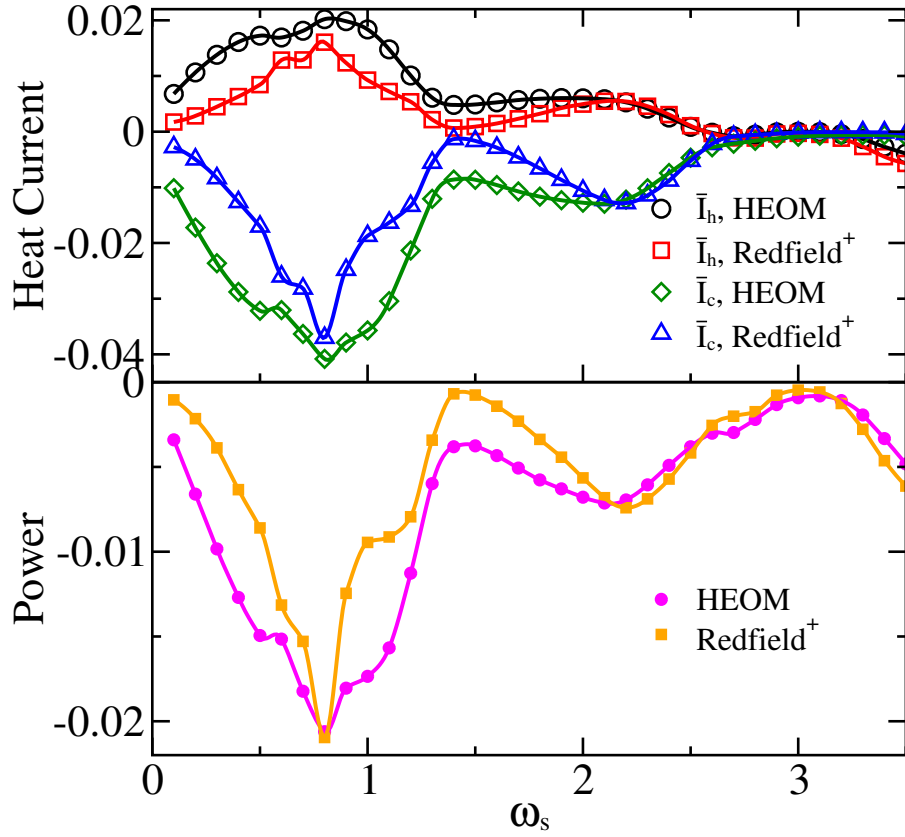


Figure 6. Mean heat currents \bar{I}_h and \bar{I}_c according to Redfield⁺ and HEOM (top) and the corresponding net power with the temperature gradient reversed compared to Fig. 5, i.e. the slow bath is hot, the fast bath is cold. The simulation parameters are (in a.u.): $\omega_0 = 3.0$, $\lambda = 1.0$, $\kappa_\alpha = 1.0$, $(\Omega_s, T_h) = (2.0, 2.0)$, and $(\Omega_f, T_c) = (4.0, 0.0)$.

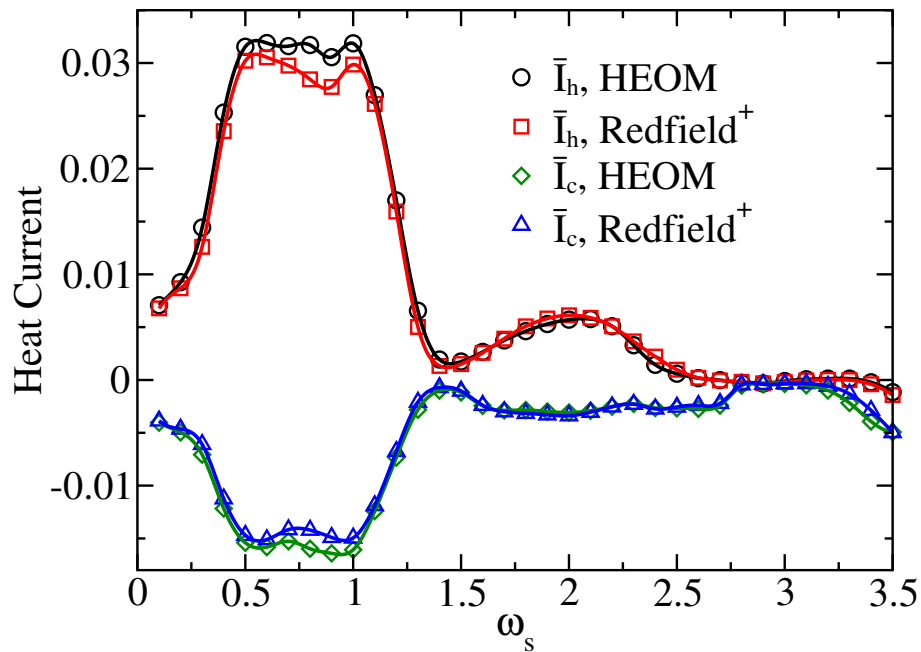


Figure 7. Same as in Fig. 5 but with larger modulation amplitude $\lambda = 1.5$.

4.2. Resonance analysis

We wish to understand the behavior of the heat currents when the driving frequency ω_s is varied and thus, to get an insight into the periodic steady state dynamics of the thermal machine. We here show that under slow to moderate driving the weak coupling master equation is applicable with the reservoirs staying in or close to thermal equilibrium while under faster driving they are pushed towards nonequilibrium with strong WM-reservoir correlations.

Let us first recall the relevant time scales in the periodic steady state, i.e. the external modulation period $\tau_s = 2\pi/\omega_s$ and the typical correlation time (memory time) of the thermal reservoirs τ_R . For standard ohmic spectral distributions, $\tau_R \sim \beta$ so that at sufficiently low temperatures the reservoir relaxation time exceeds the driving period $\tau_s \ll \tau_R$. For the bandgap environment considered here, additional time scales come into play, namely, the central band frequencies Ω_α and respective widths Δ_α . Hence, one expects the individual reservoir modes to follow the external driving as long as their frequency ω_s is sufficiently smaller than Ω_α , while collective response emerges if this is no longer true.

To develop a qualitative understanding, we consider the regime of weak coupling (where the Born-Markov approximation is presumably valid). The interaction between the WM and the reservoirs is then governed by the real-valued transition rates

$$\Gamma_{0/1}^{(k)} = \frac{\lambda^2}{4\omega_s^2} [S_h(\mp\omega^{(k)}) + S_c(\mp\omega^{(-k)})]$$

which directly determine the heat fluxes (cf. Appendix). Consequently, the reservoirs are only probed at the central ($\omega^{(0)} = \omega_0$) and sideband ($\omega^{(k)}, |k| \neq 0$) resonances, where only the sidebands contribute to the heat current and the contribution of each sideband is weighted by the Bessel function $J_k(\lambda/\omega_s)$, see Eq. (4). The underlying approximation requires that $\omega_s \ll \omega_0, \Omega_\alpha$.

This treatment leads to the prediction that for the distributions of Eq. (8) around Ω_α , we expect a resonance-like pattern for the heat currents around $\omega^{(k)} \approx \Omega_\alpha$ and thus around the driving frequencies

$$\omega_s^{(k)} = \frac{|\Omega_\alpha - \omega_0|}{k}, \quad k = 1, 2, 3, \dots \quad (30)$$

In Fig. 5 this Markovian prediction for the heat current is shown together with the prediction from Redfield⁺ and HEOM. For the parameters chosen ($\lambda = |\Omega_\alpha - \omega_0| = 1$), all treatments yield pronounced resonances around $\omega_s^{(1)} = 1$ (single-quantum exchange) and $\omega_s^{(1)} = 1/2$ (two-quanta exchange). However, the accuracy of the Markovian description is rather poor: the precise location of the resonance is shifted from the Markovian resonance condition and the peak heights differ substantially from the exact ones. The Markovian approximation completely fails in the limit $\omega_s \rightarrow 0$. In a more accurate description, higher order quanta-exchange resonances are blurred by the steep decrease

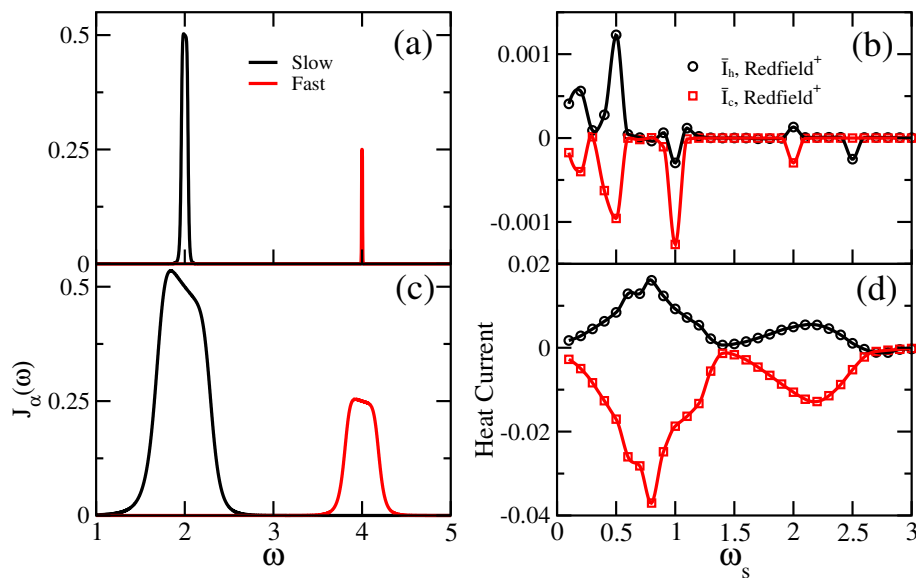


Figure 8. Spectral distributions of slow and fast reservoirs for narrow bandwidths (panel (a) given by Eq. (34)) and for broad bandwidth (panel (c) given by Eq. (8)). Panel (b) and panel (d) show the corresponding heat current modulated by driving frequency ω_s . The simulation parameters are (in a.u.): $\omega_0 = 3.0$, $\lambda = 1.0$, $\kappa_\alpha = 1.0$, $(\Omega_s, T_h) = (2.0, 2.0)$, and $(\Omega_f, T_c) = (4.0, 0.0)$.

of the heat currents towards $\omega_s \rightarrow 0$. Apparently, the resonances are broadened by the finite bandwidths of the reservoirs of order $\Delta_\alpha/2k$, see Figs. 5–7.

Memory effects become even more prominent when the temperature gradient is reversed as in Fig. 6, where the high frequency reservoir has $T_c = 0$. This induces much stronger memory effects (non-Markovian behavior) on time scales of order τ_s so that (i) resonances occur slightly away from $\omega_s^{(k)}$ and (ii) higher order system-reservoir correlations cannot be neglected. They broaden the resonances and increase their magnitudes, thus, demonstrating that ‘deep’ quantum effects *enhance* the heat transfer. With increasing driving amplitude, see Fig. 7, $\omega(t)$ covers the full bandwidths of the reservoirs, i.e. $\max_t\{\omega(t)\} \approx \Omega_f + \Delta_f/2$, $\min_t\{\omega(t)\} \approx \Omega_s - \Delta_s/2$, so that resonances overlap.

While the previous analysis reveals the behavior for slow to moderate driving frequencies, we also observe broad extrema in the heat currents for driving frequencies $\omega_s > \omega_s^{(1)}$, e.g. around $\omega_s = 2$. They cannot be understood from a strictly Markovian treatment since they lie outside the range of the resonance condition (30). To explain their nature, we consider the limit, where the two reservoirs collapse to single oscillator modes with frequencies Ω_α . Accordingly, one has

$$H_{\text{harmonic}}(t) = \omega(t)\sigma_+\sigma_- + \sum_\alpha \left\{ \frac{p_\alpha^2}{2} + \frac{1}{2}\Omega_\alpha^2 q_\alpha^2 - c_\alpha q_\alpha \sigma_x \right\} \quad (31)$$

with the corresponding Heisenberg equations of motion

$$\ddot{q}_\alpha(t) + \Omega_\alpha^2 q_\alpha(t) = c_\alpha \sigma_x(t) ; \quad (32a)$$

$$\dot{\sigma}_x(t) + \omega(t)\sigma_y(t) = 0 ; \quad (32b)$$

$$\dot{\sigma}_y(t) - \omega(t)\sigma_x(t) - 2[c_f q_f(t) + c_s q_s(t)]\sigma_z(t) = 0 ; \quad (32c)$$

$$\dot{\sigma}_z(t) + 2[c_f q_f(t) + c_s q_s(t)]\sigma_y(t) = 0 . \quad (32d)$$

One can iterate the above equations to obtain for the reservoir oscillator modes

$$\begin{aligned} \ddot{q}_\alpha(t) + \Omega_\alpha^2 q_\alpha(t) + 2c_\alpha^2 \int_0^t du \int_0^u ds \omega(s)\sigma_z(s) q_\alpha(s) \\ = -c_\alpha \int_0^t du \omega(u) \int_0^u ds [\omega(s)\sigma_x(s) + 2c_{\bar{\alpha}} q_{\bar{\alpha}}(s)\sigma_z(s)] . \end{aligned} \quad (33)$$

with the index $\bar{\alpha} = f, s$ for $\alpha = s, f$. To order c_α^2 , this equation describes linearly and parametrically driven harmonic systems while higher order couplings induce nonlinearities.

The time dependent heat current follows according to (26) from $I_\alpha(t) \propto c_\alpha \langle \sigma_y q_\alpha \rangle_t$. Since to leading order $\langle q_\alpha \rangle_\alpha = 0$, the c_α -dependent terms in Eq. (32c) for $\sigma_y(t)$ are relevant which implies $I_\alpha \propto c_\alpha^2 \langle q_\alpha(t) q_\alpha(s) \sigma_z(s) \rangle$. Thus, to second order $\sigma_z(t)$ carries frequencies $\omega^{(k)}$ and one regains the resonance condition Eq. (30) for the time averaged heat current. Beyond this approximation, the coupled dynamics Eqs. (32) and (33) describes oscillatory behavior at frequencies $\omega^{(k)}, n\Omega_s, m\Omega_f$ (n, m being integer) and their combinations, thus giving rise to beating between WM and the reservoirs as well as between the reservoirs. Hence, in the time averaged heat current we expect in the range $\omega_s > \omega_s^{(1)}$ leading order resonances behavior at the frequencies $\omega_s \approx \Omega_\alpha, 2\Omega_\alpha$, at $\omega_s = (\omega_0 + \Omega_\alpha)/2$ and $\omega_s \approx (\Omega_f \mp \Omega_s)/2$.

The above picture can be conveniently verified by considering narrow spectral distributions of the form

$$J_\alpha(\omega) = \frac{\kappa_\alpha \omega}{(\omega^4 - \Omega_\alpha^4)^6 + \omega^2} , \quad \alpha = s, f , \quad (34)$$

which effectively describe weakly damped oscillator modes with effective damping rates (spectral widths) $\Delta_\alpha \ll \Omega_\alpha$, see Fig. 8(a). Corresponding results for the heat current are shown in Fig. 8(b): resonant structures are found for $\omega_s > 1$ at $\omega_s = \Omega_s = 2$ and $\omega_s = (\omega_0 + \Omega_s)/2 = 2.5$. A broader spectral bandwidth of the individual reservoirs washes out individual resonances as seen in Figs. 8(c) and (d). The symmetry $|\omega_0 - \Omega_f| = \omega_0 - \Omega_s$ is broken in Fig. 9 where extrema are in complete agreement with the above predictions.

Of particular interest are reservoir-reservoir correlations that we expect to emerge in the domain of strong non-equilibrium, i.e. for $\omega_s > \omega_s^{(1)}$. As Fig. 10 reveals, in the latter range these correlations are continuously built up with increasing modulation frequency approaching a constant level in contrast to slow and moderate modulation, where these correlations only appear near resonances. Note that $\langle X_s X_f \rangle$ -correlations do not exist in the Born-Markov approximation (which is a perturbative treatment up to order c_α^2 in the secular approximation). These correlations reflect higher order system-bath contributions, at least of order c_α^4 , where they match the size of higher order contributions of auto-correlations (cf. the normalization in Eq. (27)).

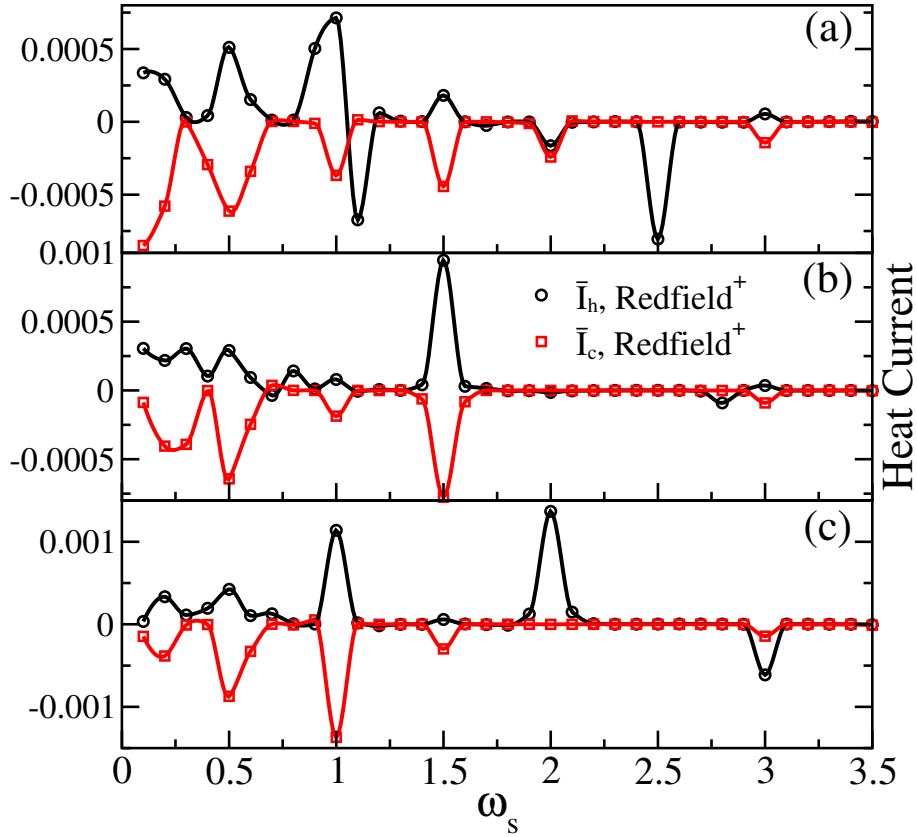


Figure 9. Mean heat currents as a function of modulation frequency for narrow bandwidth reservoirs as in Fig. 8 but for (a) $\omega_0 = 3.0$, $\lambda = 2.0$; (b) $\omega_0 = 3.5$, $\lambda = 1.5$; (c) $\omega_0 = 4.0$, $\lambda = 2.0$. Other parameters are (in a.u.) $\kappa_\alpha = 1.0$, $(\Omega_s, T_h) = (2.0, 2.0)$, and $(\Omega_f, T_c) = (5.0, 0.0)$.

The following picture emerges from the above analysis is thus this: for slow and moderate driving the WM exchanges energy with the thermal reservoirs via multi-sideband resonances, while for faster modulation the reservoirs are driven out of equilibrium with a complex resonance pattern. Finite bandwidth of the environment induces broadening of the extrema in the heat currents. One may thus expect that operation as a heat engine is only possible in the slow-moderate driving regime, while our setting turns into a mere dissipator for sufficiently fast driving. This is largely true but the heat engine operation also depends on the temperature gradient as we will see in the next section.

4.3. Power and efficiency

The operation of the thermal machine as a heat engine is characterized by its power output and its efficiency. In steady-state, the power can be calculated directly from

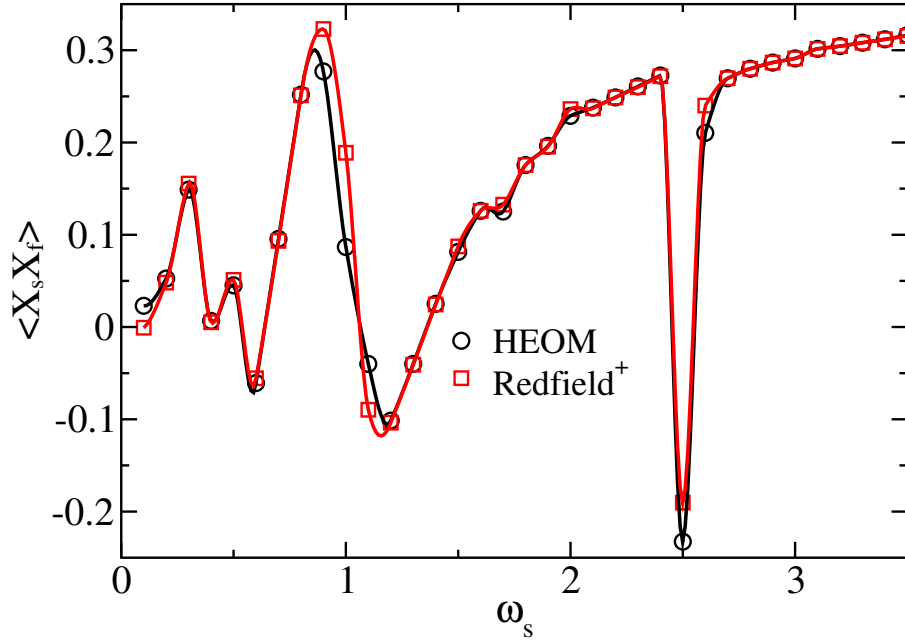


Figure 10. Time averaged reservoir-reservoir correlation [cf. Eq. (27)] as a function of the modulation frequency simulated by HEOM and Redfield⁺. The simulation parameters are the same as in Fig. 9(a).

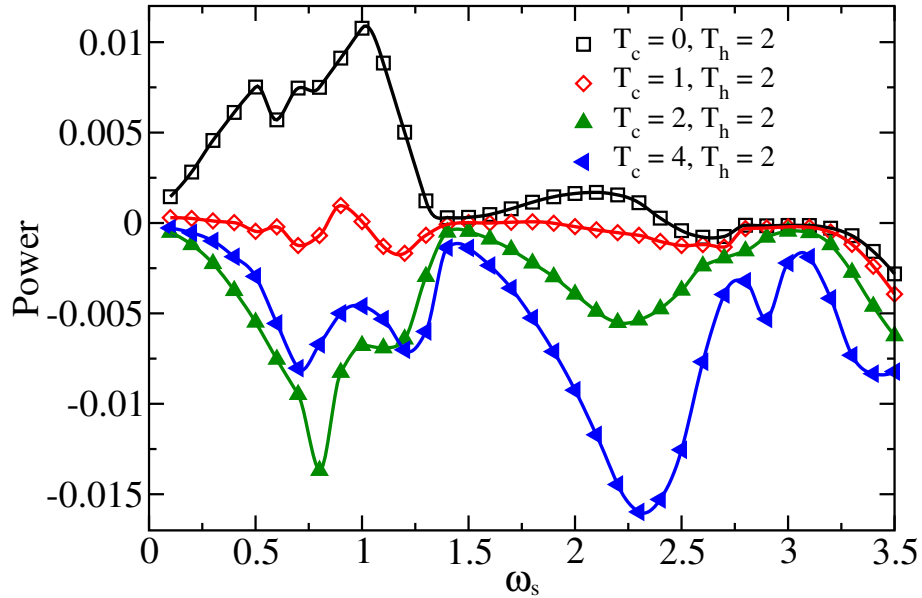


Figure 11. Net power output as a function of the modulation frequency for various temperature gradients with T_c allocated to the slow reservoir and T_h to the fast one. The simulation parameters are (in a.u.): $\omega_0 = 3.0$, $\lambda = 1.0$, $\kappa_\alpha = 1.0$, $\Omega_s = 2.0$, and $\Omega_f = 4.0$.

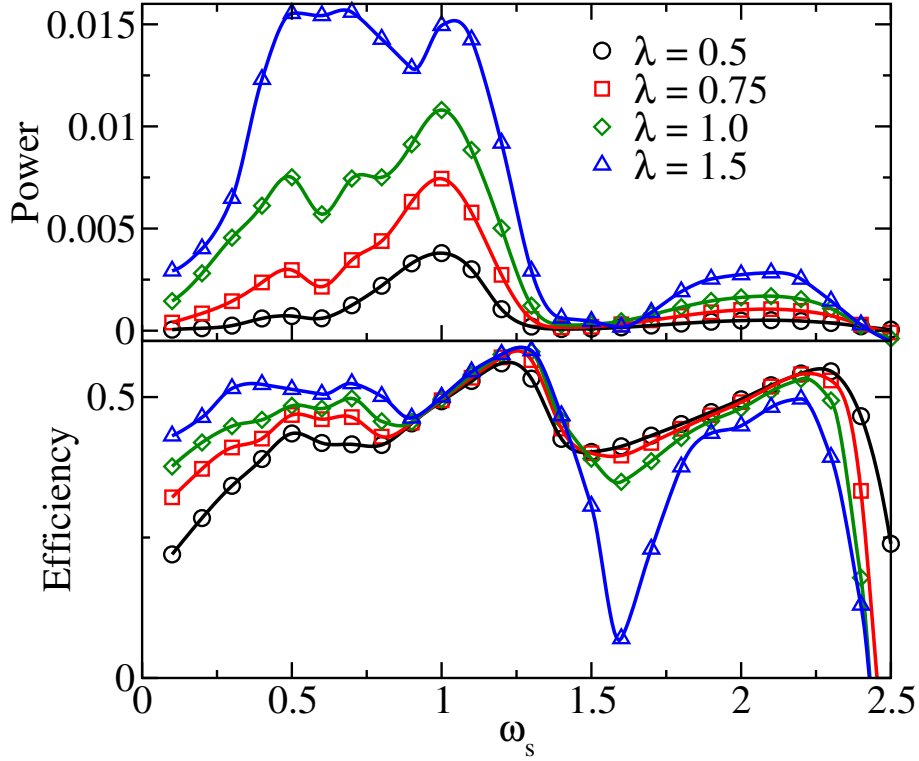


Figure 12. Net power and efficiency versus the driving frequency for various driving amplitudes. The simulation parameters are (in a.u.): $\omega_0 = 3.0$, $\kappa_\alpha = 1.0$, $(\Omega_s, T_0) = (2.0, 0.0)$, and $(\Omega_f, T_h) = (4.0, 2.0)$.

$\bar{I}_s(t)$ and $\bar{I}_f(t)$ according to

$$\begin{aligned}
 P &= \lim_{t \rightarrow \infty} \frac{1}{\tau_s} \int_t^{t+\tau_s} d\tau \left\langle -\frac{\partial H_s(\tau)}{\partial \tau} \right\rangle = \lim_{t \rightarrow \infty} \frac{1}{\tau_s} \int_t^{t+\tau_s} d\tau \omega(\tau) \dot{P}_1(\tau) \\
 &= \lim_{t \rightarrow \infty} \frac{i}{\tau_s} \sum_k \int_t^{t+\tau_s} d\tau \omega(\tau) [\rho_{\mathbf{0}_k^+}^{12}(\tau) - \rho_{\mathbf{0}_k^+}^{21}(\tau)] \\
 &= \lim_{t \rightarrow \infty} \frac{1}{\tau_s} \int_t^{t+\tau_s} d\tau [I_c(\tau) + I_h(\tau)] = \bar{I}_c + \bar{I}_h .
 \end{aligned} \tag{35}$$

Here, $\rho_{\mathbf{0}_k^+}^{12}$ and $\rho_{\mathbf{0}_k^+}^{21}$ denote ADO elements and $P_1(t) = \langle \sigma_+ \sigma_- \rangle_t$ denotes the excited state population. From the above definition positive values of P mean that heat is converted into work (heat engine operation), while negative P means that work is dissipated in the reservoirs (dissipator). In steady-state, a formal definition of the efficiency is given by

$$\eta = \frac{P}{I_{\bar{\alpha}}} = 1 - \left| \frac{\bar{I}_\alpha}{\bar{I}_{\bar{\alpha}}} \right| \leq 1 , \tag{36}$$

where α ($\bar{\alpha}$) refers to the slow or the fast reservoir at temperature T_c (T_h). Note that here the efficiency has a physical meaning only for positive values and is then a figure of merit for the heat engine. In parameter domains where the increase of \bar{I}_h exceeds that of \bar{I}_c , the efficiency increases as well.

We start with the power dependence on the driving frequency for various temperature gradients in Fig. 11. Upon increasing the temperature of the slow reservoir while in parallel decreasing that of the fast reservoir, the power turns from positive values to negative ones. The resonance pattern is clearly seen and demonstrates relatively high power supply of the heat engine at the one-quantum resonance $\omega_s \approx |\Omega_\alpha - \omega_0|$. For equal temperatures of both reservoirs or higher temperatures of the low energy (slow bath) reservoir, the machine operates as a dissipator. Interesting is the strong dissipation found for $T_c = 4, T_h = 2$ (slow bath, fast bath) around $\omega_s \approx 2 = \Omega_s$, which supports the above statement within the Rabi model of effective energy transfer towards the low frequency reservoir.

In the domain of heat engine operation, power and efficiency are shown in Fig. 12 for various driving amplitudes. The general result is that stronger driving leads to larger power output and enhanced efficiencies only for slow to moderate driving $\omega_s \lesssim 1$, where sideband resonances occur. For faster driving, the situation is reversed: weaker driving implies higher efficiencies which is compatible with the tendency of the machine to turn into a dissipator (at the highest driving frequencies, where $\eta \rightarrow 0$). Interestingly, around the single-quantum resonance the efficiency is basically independent of the driving strength and reaches values up to about 60%. However, most remarkably, even in a situation with basically *no* spectral overlap, i.e. $\lambda = 0.5$ so that the modulation $\omega(t)$ always remains within the bandgap between the reservoirs, we find substantial heat power with high efficiency. This nicely illustrates the important role of the sidebands due to the periodic driving.

The dependence of the power and the efficiency on the coupling strength between WM and the reservoirs is depicted in Fig. 13. The power output increases with the coupling strength exhibiting growing resonances. The corresponding efficiency, however, decreases with the coupling strength only in the adiabatic regime of very slow driving but remains basically unaffected for faster modulation.

5. Conclusion

This paper has studied a minimal model for a quantum heat engine in a non-trivial setting: By periodically modulating the transition frequency of a TLS acting as WM, this WM is in alternating spectral overlap with a cold or a hot reservoir with localized and disjunct spectra. It simplifies conventional designs, for example the four stroke Otto engine, since no explicit switching on-off of the coupling between WM and the reservoirs is necessary. It also extends previous proposals [4] to operate under shorter cycle times with no need for coupling/de-coupling from the reservoirs after several modulation periods. Theoretical predictions have been obtained based on the formally exact HEOM simulation technique and its comparison with perturbative treatments.

We find that the perturbative Redfield⁺ can provide quantitatively correct predictions of the heat flux behaviour and the quantum heat engine performance even in 'deep' quantum regime. The resonance-like pattern in the domain of heat engine

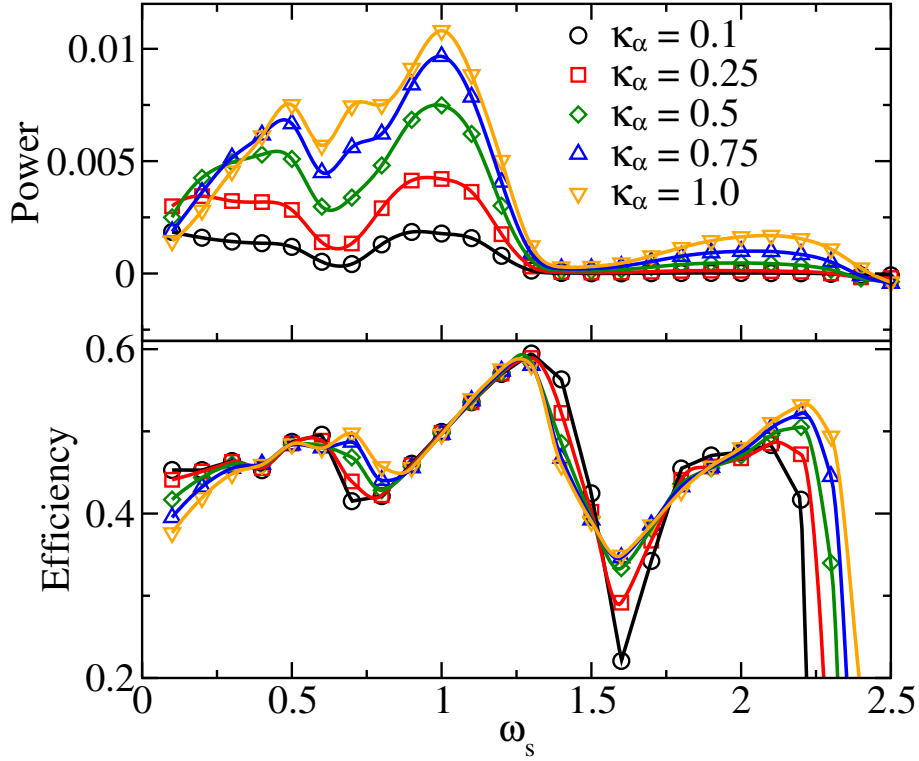


Figure 13. Net power and efficiency versus the driving frequency for various thermal coupling strengths of the WM with the reservoirs. The driving amplitude $\lambda = 1.0$, and other parameters are as in Fig. 12.

operation shows a strong dependence on the driving frequency: for slow and moderate driving the WM exchanges energy with thermal reservoirs via multi-sideband resonances, while for faster modulation the reservoirs are driven out of equilibrium with a complex resonance pattern. Finite bandwidth of the environment induces broadening of the extrema in the heat currents.

The driving amplitude as well as the WM-reservoir interaction play a decisive role in determining the quantum heat engine power output but a lesser role in determining its efficiency. Interestingly, the heat engine can still operate even under fast driving which may provide a new pathway to the design of quantum heat engines.

Acknowledgment

We thank Michael Wiedmann, Ronzani Alberto, and Jukka P. Pekola for fruitful discussion. M. X. acknowledges support by the state of Baden-Württemberg through bwHPC (JUSTUS 2 cluster). This work has been supported by IQST and the German Science Foundation (DFG) under AN336/12-1 (For2724). G.K. acknowledges support of the PACE IN Quanterra project, the ISF, and the NSF-BSF.

Author contributions

M. X. performed numerical simulations. All authors have been involved in model setting, results analysis, discussion of scientific results and in the writing of the manuscript.

Data availability

All the data that support the figures within this article are available from the corresponding author upon reasonable request.

Appendix: Heat flux in Born-Markov approximation

The population dynamics of a driven two level system interacting with a bandgap reservoir as considered in the main text is governed by [4]

$$\begin{aligned} \frac{d}{dt}P_0(t) &= \Gamma_0[1 - P_0(t)] - \Gamma_1P_0(t) \\ &= -[\Gamma_0 + \Gamma_1]P_0(t) + \Gamma_0 \quad , \end{aligned} \quad (37)$$

and $P_1(t) = 1 - P_0(t)$. Asymptotically for $\dot{P}_i(t) = 0$, this equation can be solved as

$$P_i = \frac{\Gamma_i}{\Gamma_0 + \Gamma_1} \quad , i = 0, 1 \quad (38)$$

with transition rates $\Gamma_{0/1} = \sum_k \Gamma_{0/1}^{(k)}$, where

$$\Gamma_{0/1}^{(k)} = \frac{\lambda^2}{4\omega_s^2} [S_h(\mp\omega^{(k)}) + S_c(\mp\omega^{(-k)})] \quad . \quad (39)$$

Accordingly, the heat currents in steady state are given by

$$I_h(\omega_s) = \frac{\lambda^2}{4\omega_s^2} \sum_k \omega^{(k)} S_h(\omega^{(k)}) \frac{e^{-\beta_h\omega^{(k)}} - w}{w + 1} \quad ; \quad (40a)$$

$$I_c(\omega_s) = \frac{\lambda^2}{4\omega_s^2} \sum_k \omega^{(k)} S_c(\omega^{(-k)}) \frac{e^{-\beta_c\omega^{(-k)}} - w}{w + 1} \quad , \quad (40b)$$

with $\omega^{(k)}$ as in Eq. (4) and the population ratio

$$w(\omega_s) = \frac{P_1}{P_0} = \frac{\Gamma_0}{\Gamma_1} \quad . \quad (41)$$

References

- [1] Benenti G, Casati G, Saito K and Whitney R S 2017 *Phys. Rev.* **694** 1–124
- [2] Binder F, Correa L A, Gogolin C, Anders J and Adesso G (eds) 2018 *Thermodynamics in the Quantum Regime: Fundamental Aspects and New Directions (Fundamental Theories in Physics vol 195)* (Springer, Berlin)

- [3] Klatzow J, Becker J N, Ledingham P M, Weinzetl C, Kaczmarek K T, Saunders D J, Nunn J, Walmsley I A, Uzdin R and Poem E 2019 *Phys. Rev. Lett.* **122** 110601
- [4] Mukherjee V, Kofman A G and Kurizki G 2020 *Commun. Phys.* **3** 1–12
- [5] Wiedmann M, Stockburger J T and Ankerhold J 2020 *New. J. Phys.* **22** 033007
- [6] Wiedmann M, Stockburger J T and Ankerhold J 2021 *Eur. Phys. J. Spec. Top.* 1–7
- [7] Uzdin R, Levy A and Kosloff R 2015 *Phys. Rev. X* **5** 031044
- [8] Restrepo S, Cerrillo J, Bastidas V M, Angelakis D G and Brandes T 2016 *Phys. Rev. Lett.* **117** 250401
- [9] Weiss U 2012 *Quantum dissipative systems* 4th ed (New Jersey: World Scientific)
- [10] Tanimura Y and Kubo R 1989 *J. Phys. Soc. Jpn.* **58** 101
- [11] Xu M, Stockburger J and Ankerhold J 2021 *Phys. Rev. B* **103** 104304
- [12] Motz T, Wiedmann M, Stockburger J T and Ankerhold J 2018 *New. J. Phys.* **20** 113020
- [13] Stockburger J T and Grabert H 2002 *Phys. Rev. Lett.* **88** 170407
- [14] Yang C H and Wang H 2020 *Entropy* **22** 1099
- [15] Velizhanin K A, Wang H and Thoss M 2008 *Chem. Phys. Lett.* **460** 325–330
- [16] Wang H and Thoss M 2003 *J. Chem. Phys.* **119** 1289–1299
- [17] Yamamoto T, Kato M, Kato T and Saito K 2018 *New. J. Phys.* **20** 093014
- [18] Gull E, Millis A J, Lichtenstein A I, Rubtsov A N, Troyer M and Werner P 2011 *Rev. Mod. Phys.* **83** 349
- [19] Roßnagel J, Dawkins S T, Tolazzi K N, Abah O, Lutz E, Schmidt-Kaler F and Singer K 2016 *Science* **352** 325–329
- [20] Cottet N, Jezouin S, Bretheau L, Campagne-Ibarcq P, Ficheux Q, Anders J, Auffèves A, Azouit R, Rouchon P and Huard B 2017 *Proc. Natl. Acad. Sci. USA* **114** 7561–7564
- [21] Pekola J P 2015 *Nat. Phys.* **11** 118–123
- [22] Ronzani A, Karimi B, Senior J, Chang Y C, Peltonen J T, Chen C and Pekola J P 2018 *Nat. Phys.* **14** 991–995
- [23] Senior J, Gubaydullin A, Karimi B, Peltonen J T, Ankerhold J and Pekola J P 2020 *Commun. Phys.* **3** 1–5
- [24] Meschke M, Guichard W and Pekola J P 2006 *Nature* **444** 187–190
- [25] Pascal L M A, Courtois H and Hekking F W J 2011 *Phys. Rev. B* **83** 125113
- [26] Schwab K, Henriksen E, Worlock J and Roukes M L 2000 *Nature* **404** 974–977
- [27] Chang C W, Okawa D, Majumdar A and Zettl A 2006 *Science* **314** 1121–1124
- [28] Pruttivarasin T, Ramm M, Talukdar I, Kreuter A and Häffner H 2011 *New. J. Phys.* **13** 075012
- [29] Kosloff R and Levy A 2014 *Annu. Rev. Phys. Chem.* **65** 365–393

- [30] Gelbwaser-Klimovsky D, Niedenzu W and Kurizki G 2015 *Advances In Atomic, Molecular, and Optical Physics* **64** 329–407
- [31] Anders J and Giovannetti V 2013 *New. J. Phys.* **15** 033022
- [32] Perarnau-Llobet M, Wilming H, Riera A, Gallego R and Eisert J 2018 *Phys. Rev. Lett.* **120**(12) 120602 URL <https://link.aps.org/doi/10.1103/PhysRevLett.120.120602>
- [33] Lobejko M, Mazurek P and Horodecki M 2020 *Quantum* **4** 375
- [34] Gelbwaser-Klimovsky D, Alicki R and Kurizki G 2013 *Phys. Rev. E* **87** 012140
- [35] Naseem M T, Misra A, Müstecaplıoğlu Ö E and Kurizki G 2020 *Phys. Rev. Research* **2** 033285
- [36] Gelbwaser-Klimovsky D and Kurizki G 2015 *Sci. Rep.* **5** 1–6
- [37] Gelbwaser-Klimovsky D and Kurizki G 2014 *Phys. Rev. E* **90** 022102
- [38] Ghosh A, Gelbwaser-Klimovsky D, Niedenzu W, Lvovsky A I, Mazets I, Scully M O and Kurizki G 2018 *Proc. Natl. Acad. Sci. USA* **115** 9941–9944
- [39] Kofman A, Kurizki G and Sherman B 1994 *J. Mod. Opt.* **41** 353–384
- [40] Lambropoulos P, Nikolopoulos G M, Nielsen T R and Bay S 2000 *Rep. Prog. Phys.* **63** 455
- [41] Tanimura Y 2006 *J. Phys. Soc. Jpn.* **75** 082001–082039
- [42] Tanimura Y 2020 *J. Chem. Phys.* **153** 020901
- [43] Kato A and Tanimura Y 2015 *J. Chem. Phys.* **143** 064107
- [44] Song L and Shi Q 2017 *Phys. Rev. B* **95** 064308
- [45] Feynman R P and Vernon F L 1963 *Ann. Phys.* **24** 118
- [46] Magazzù L, Denisov S and Hänggi P 2017 *Phys. Rev. A* **96** 042103
- [47] Magazzù L, Denisov S and Hänggi P 2018 *Phys. Rev. E* **98** 022111
- [48] Grifoni M and Hänggi P 1998 *Phys. Rev.* **304** 229–354
- [49] Magazzù L, Forn-Díaz P, Belyansky R, Orgiazzi J L, Yurtalan M, Otto M R, Lupascu A, Wilson C and Grifoni M 2018 *Nat. Commun.* **9** 1–8
- [50] Traversa F L, Di Ventra M and Bonani F 2013 *Phys. Rev. Lett.* **110** 170602
- [51] Levy A and Kosloff R 2014 *Europhys. Lett.* **107** 20004
- [52] Paauw F, Fedorov A, Harmans C M and Mooij J 2009 *Phys. Rev. Lett.* **102** 090501
- [53] Tanimura Y 2014 *J. Chem. Phys.* **141** 044114
- [54] Song L and Shi Q 2015 *J. Chem. Phys.* **143** 194106
- [55] Echave J and Clary D C 1992 *Chem. Phys. Lett.* **190** 225
- [56] Jin J S, Zheng X and Yan Y J 2008 *J. Chem. Phys.* **128** 234703–234717
- [57] Tang Z, Ouyang X, Gong Z, Wang H and Wu J 2015 *J. Chem. Phys.* **143** 224112
- [58] Meier C and Tannor D 1999 *J. Chem. Phys.* **111** 3365
- [59] Ishizaki A and Tanimura Y 2005 *J. Phys. Soc. Jpn.* **74** 3131–3134

- [60] Xu M, Song L, Song K and Shi Q 2017 *J. Chem. Phys.* **146** 064102
- [61] Zhang H D, Cui L, Gong H, Xu R X, Zheng X and Yan Y 2020 *J. Chem. Phys.* **152** 064107
- [62] Ikeda T and Scholes G D 2020 *J. Chem. Phys.* **152** 204101
- [63] Yan Y, Xing T and Shi Q 2020 *J. Chem. Phys.* **153** 204109
- [64] Tanimura Y 1990 *Phys. Rev. A* **41** 6676
- [65] Shi Q, Chen L P, Nan G J, Xu R X and Yan Y J 2009 *J. Chem. Phys.* **130** 084105–084108
- [66] Cui L, Zhang H D, Zheng X, Xu R X and Yan Y 2019 *J. Chem. Phys.* **151** 024110
- [67] Shi Q, Xu Y, Yan Y and Xu M 2018 *J. Chem. Phys.* **148** 174102
- [68] Dunn I S, Tempelaar R and Reichman D R 2019 *J. Chem. Phys.* **150** 184109
- [69] Yan Y, Xu M, Li T and Shi Q 2021 *J. Chem. Phys.* **154** 194104
- [70] Breuer H P and Petruccione F 2002 *The Theory of Open Quantum Systems* (New York: Oxford University Press)
- [71] Frishman E and Shapiro M 1996 *Phys. Rev. A* **54**(4) 3310–3321
- [72] Thanopoulos I, Brumer P and Shapiro M 2008 *J. Chem. Phys.* **129** 194104
- [73] Xu M, Yan Y, Liu Y and Shi Q 2018 *J. Chem. Phys.* **148** 164101
- [74] Trushechkin A 2019 *Lobachevskii J. Math.* **40** 1606–1618
- [75] Zhu L, Liu H, Xie W and Shi Q 2012 *J. Chem. Phys.* **137** 194106
- [76] Kato A and Tanimura Y 2016 *J. Chem. Phys.* **145** 224105
- [77] Duan C, Hsieh C Y, Liu J, Wu J and Cao J 2020 *J. Phys. Chem. Lett.* **11** 4080–4085
- [78] Wang J S, Agarwalla B K, Li H and Thingna J 2014 *Front. Phys.* **9** 673–697